

Statistical parameters of random heterogeneity estimated by analysing coda waves based on finite difference method

K. Emoto,* T. Saito and K. Shiomi

National Research Institute for Earth Science and Disaster Resilience, Tsukuba, Ibaraki 305-0006, Japan. E-mail: emoto@zisin.gp.tohoku.ac.jp

Accepted 2017 September 14. Received 2017 September 13; in original form 2017 March 17

SUMMARY

Short-period (<1 s) seismograms are strongly affected by small-scale (<10 km) heterogeneities in the lithosphere. In general, short-period seismograms are analysed based on the statistical method by considering the interaction between seismic waves and randomly distributed small-scale heterogeneities. Statistical properties of the random heterogeneities have been estimated by analysing short-period seismograms. However, generally, the small-scale random heterogeneity is not taken into account for the modelling of long-period (>2 s) seismograms. We found that the energy of the coda of long-period seismograms shows a spatially flat distribution. This phenomenon is well known in short-period seismograms and results from the scattering by small-scale heterogeneities. We estimate the statistical parameters that characterize the small-scale random heterogeneity by modelling the spatiotemporal energy distribution of long-period seismograms. We analyse three moderate-size earthquakes that occurred in southwest Japan. We calculate the spatial distribution of the energy density recorded by a dense seismograph network in Japan at the period bands of 8–16 s, 4–8 s and 2–4 s and model them by using 3-D finite difference (FD) simulations. Compared to conventional methods based on statistical theories, we can calculate more realistic synthetics by using the FD simulation. It is not necessary to assume a uniform background velocity, body or surface waves and scattering properties considered in general scattering theories. By taking the ratio of the energy of the coda area to that of the entire area, we can separately estimate the scattering and the intrinsic absorption effects. Our result reveals the spectrum of the random inhomogeneity in a wide wavenumber range including the intensity around the corner wavenumber as $P(m) = 8\pi \varepsilon^2 a^3 / (1 + a^2 m^2)^2$, where $\varepsilon = 0.05$ and $a = 3.1$ km, even though past studies analysing higher-frequency records could not detect the corner. Finally, we estimate the intrinsic attenuation by modelling the decay rate of the energy. The method proposed in this study is suitable for quantifying the statistical properties of long-wavelength subsurface random inhomogeneity, which leads the way to characterizing a wider wavenumber range of spectra, including the corner wavenumber.

Key words: Numerical modelling; Wave propagation; Wave scattering and diffraction.

1 INTRODUCTION

A small-scale velocity inhomogeneity generates coda waves and decreases the peak amplitude of the direct phase due to the scattering of seismic waves. These effects are important for the propagation of short-period seismic waves as well as the intrinsic attenuation. It is difficult to deterministically model the entire waveform of the short-period seismogram (<~1 s) because of the lack of knowledge of the complete small-scale structure in the earth. In general, we statistically explain the characteristics of short-period seismograms. In the

statistical method, we consider an ensemble of random small-scale heterogeneities and discuss statistical quantities of wave propagation. Using the high sensitivity of short-period seismograms to the small-scale velocity fluctuation, statistical parameters of the fluctuation in the lithosphere have been estimated (see Sato *et al.* 2012). Conversely, we usually do not take into account small-scale heterogeneities when we analyse long-period seismograms (>~2 s). For example, a 1-D layered velocity structure is often used to estimate the moment tensor of the source (e.g. Kubo *et al.* 2002). However, the nationwide dense high sensitivity seismograph network (Hi-net; Okada *et al.* 2004; Obara *et al.* 2005) revealed that, similar to short period signals, the coda of long-period seismograms is affected by small-scale heterogeneities. For example, we show the snapshot

* Now at: Graduate School of Science, Tohoku University, Sendai, Japan.

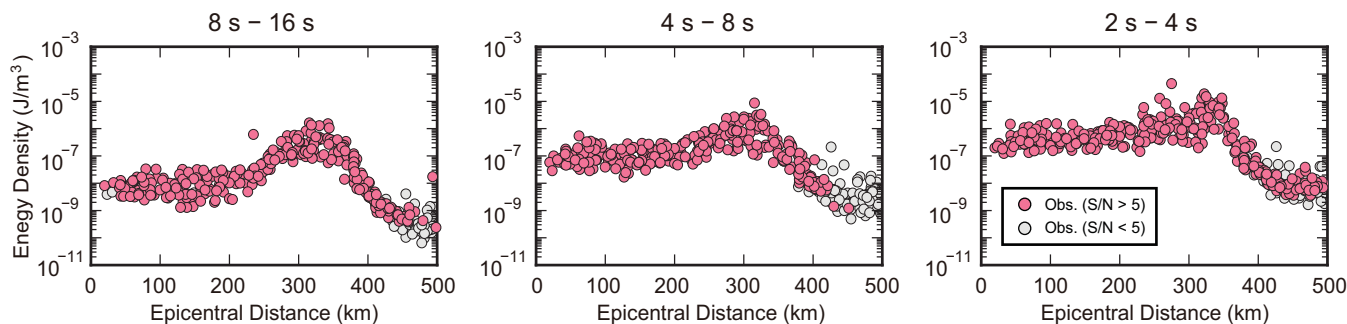


Figure 1. Energy density distribution of event 1 at the lapse time of 100 s at period bands of 8–16 s, 4–8 s and 2–4 s. Pink and grey circles indicate the station whose signal to noise ratios (S/N) of the energy density are larger and smaller than 5, respectively. The noise energy density is calculated by using the time window before the P -wave arrival time.

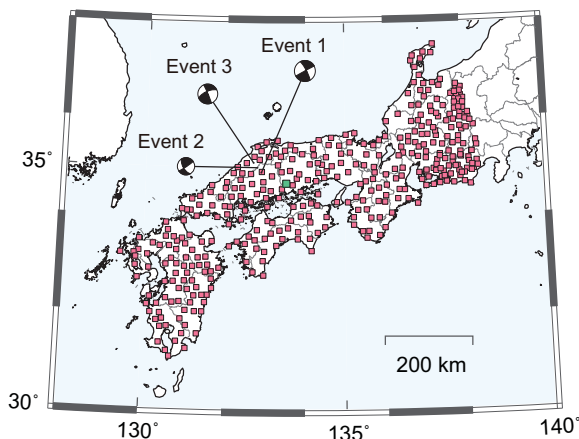


Figure 2. Map of the Hi-net stations (square) and earthquakes used in this study. The fault mechanism is obtained from the F-net moment tensor solution catalogue. The green square indicates the station N.BSEH, whose waveforms are shown in Fig. 3.

of the energy density distribution of a local earthquake in Fig. 1, recorded by the Hi-net stations shown in Fig. 2. The front of the direct wave is located at the epicentral distance between 400 and 500 km. The maximum energy can be seen at the epicentral distance between 300 and 350 km, which corresponds to the direct S or surface waves. The energy density between the source and the epicentral distance of 200 km is flat at all three period bands, which corresponds to the energy of the coda waves. The coda means the later part of the seismograms. In the spatial distribution, the energy at the epicentral distance smaller than the direct wave front corresponds to the energy of the coda waves. This uniform distribution of the energy is well known as the characteristic of short-period seismic waves resulting from wave scattering by small-scale subsurface heterogeneities (Aki 1969; Sato *et al.* 2012, fig. 1.1). This indicates that coda waves are affected by the 3-D small-scale heterogeneities even in the long period (>2 s). We note that we did not observe the coherent backscattering (Margerin *et al.* 2001; Larose *et al.* 2004; Chaput *et al.* 2015) because the station separation is not sufficiently short. Fig. 3 compares time domain waveforms and envelopes of the observed and calculated seismograms using the finite difference (FD) method with the assumption of the 1-D velocity structure. We can reproduce the main phase of the observed waveform and envelope at lapse times between 0 s and 40 s by using the 1-D structure. However, the 1-D velocity structure is not sufficient for generating the observed coda amplitude. It suggests that random inhomogeneities, whose wavelengths are shorter than the

seismic-wave wavelength, are missed in the 1-D structure. Moreover, we would be able to estimate such random inhomogeneity in the crust by analysing long-period seismic waves. One of the advantages of using the long-period seismograms to estimate small-scale heterogeneities is that we can calculate the entire waveforms by using FD simulations for long-period waves. For short-period seismic waves, statistical methods with many assumptions have been applied, such as the uniform background velocity structure, infinite space, and scalar wave (e.g. Saito *et al.* 2005). Conversely, we need fewer assumptions in the FD simulation.

To estimate the statistical properties of the medium heterogeneity, the multiple lapse time window (MLTW) method has been widely used (Fehler *et al.* 1992; Hoshiba 1993). In this method, the spatial variation of coda energies in several time windows is modelled based on the energy transport theory. To do this, we need combinations of one (or more) station(s) and multiple earthquakes or multiple stations and one (or more) earthquake(s). By using the dense seismic network, we can obtain the spatiotemporal variation of the energy field. In volcanoes, Wegler & Lühr (2001) and Yamamoto & Sato (2010) analysed the spatial variation of the energy density by using campaign observation data of active sources. On a regional scale, Asano & Saito (2011) and Saito *et al.* (2013a) analysed the spatial distribution of the energy density recorded by Hi-net stations and estimated the scattering coefficient that characterizes the small-scale heterogeneity by applying the radiative transfer theory.

In this study, we analyse the energy of longer-period seismic waves compared to previous studies to estimate the statistical parameters of small-scale heterogeneities and the intrinsic attenuation at a local scale. We use FD simulations to model the seismic wave energy rather than stochastic methods (e.g. the radiative transfer theory). We focus on the spatiotemporal distribution of the energy obtained by the dense seismic network Hi-net and extend the concept of the MLTW method.

2 DATA AND METHOD

2.1 Data

We selected three earthquakes as listed in Table 1. These events are large enough to generate high signal to noise ratios for the coda waves analysis and do not have any following aftershocks in the coda. There was an earthquake with a magnitude of 6.6 that occurred on 2016 October 21. We do not use this earthquake because some aftershocks are included at the coda of this earthquake. We use Hi-net stations within the epicentral distance of 500 km (Fig. 2) and remove the instrumental response to obtain the long-period waves

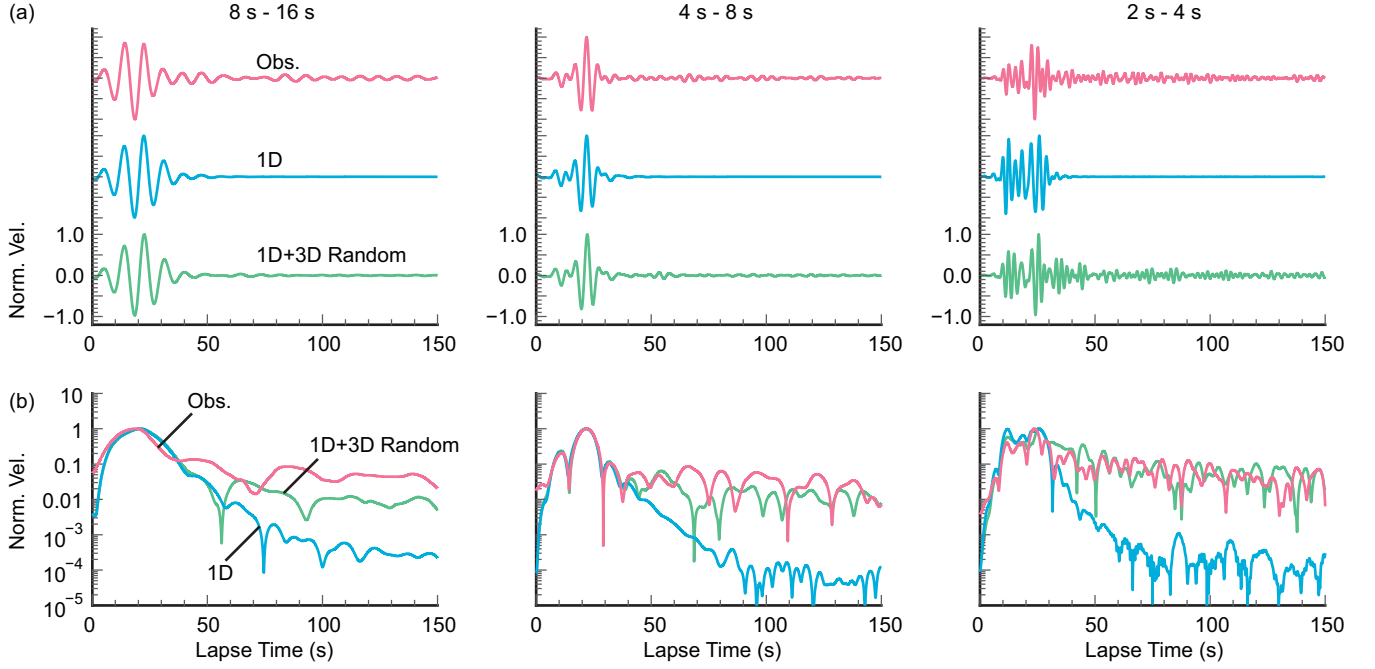


Figure 3. Comparison of the observed and calculated vertical-component waveforms for event 1 in linear (a) and semi-log (b) scales. Recorded station is N.BSEH shown by the green square in Fig. 2, whose epicentral distance is 62 km. Waveforms labelled as 1-D are waveforms calculated by assuming the 1-D velocity structure. Waveforms labelled as 1-D+3-D Random indicate calculated waveforms by adding 3-D random fluctuation in the crust to the 1-D structure, where we set the best-fit random medium parameters at each frequency band.

Table 1. List of earthquakes analysed in this study. This information is obtained from the JMA unified hypocentre catalogue.

Event ID	Date	Depth	Mag.
Event 1	2011.11.21 19:16:30	12 km	5.2
Event 2	2007.05.13 08:13:55	10 km	4.3
Event 3	2011.06.04 01:57:31	11 km	4.9

by using the method proposed by Maeda *et al.* (2011). We visually check the quality of waveforms and remove the stations for which the quality of the observed waveforms is low or the amplitude is saturated (Shiomi *et al.* 2005). We calculate the energy density at three period bands: 8–16 s, 4–8 s, and 2–4 s. The energy density is defined by summing the squared velocity seismograms of three components and multiplying it by the typical mass density as

$$E(\Delta, t) = \rho \{v_U^2(\Delta, t) + v_R^2(\Delta, t) + v_T^2(\Delta, t)\}, \quad (1)$$

where $\rho (=2.6 \times 10^3 \text{ kg m}^{-3})$ is the mass density, Δ is the epicentral distance, and $v_{U,R,T}$ denote the vertical, radial, and transverse components of the velocity seismograms, respectively.

2.2 Energy ratio

We analyse the temporal variation of the ratio of the energy of the coda to that of the entire area. In the MLTW analysis, the spatial variation of the energies of several time windows is analysed. By taking advantage of dense and wide seismic observation, we analyse the temporal change of the energy distribution in this study. The energy of the seismic wave is affected by both the scattering due to the small-scale heterogeneities and intrinsic attenuation due to the anelastic process. In the MLTW analysis, the scattering and the intrinsic attenuation are separated by analysing the behaviour of the energies in several time windows. Different time windows are differently affected by the scattering and the intrinsic

attenuation. By analysing the coherent intensity and the average of the incoherent intensity, we can also separate the intrinsic and the scattering attenuations (e.g. Ritter *et al.* 1998; De Rosny & Roux 2001; Chaput *et al.* 2015). While only coherent intensity is affected by the scattering, the intrinsic attenuation affects both intensities. In this study, we analyse the energies of the entire area and the coda to separate the scattering and intrinsic effects. We define the entire area (E_T) and coda (E_C) energies as

$$E_T(t) = \int_0^{\Delta_D(t)} 2\pi \Delta E(\Delta, t) d\Delta, \\ E_C(t) = \int_0^{\Delta_c} 2\pi \Delta E(\Delta, t) d\Delta, \quad (2)$$

where $\Delta_D(t)$ is the epicentral distance of the direct wave front. The coda energy is defined by the energy within the fixed area. The maximum epicentral distance of the coda energy is set as $\Delta_c = 50$ km. We calculate the ratio of the coda energy to the entire area energy as

$$ER(t) = \frac{E_C(t)}{E_T(t)}. \quad (3)$$

By taking the ratio, the effect of the intrinsic attenuation can be cancelled. This is because the amount of the intrinsic attenuation is controlled by how long the waves travel in the medium. At the same lapse time, both the coda and entire area energies are affected by the intrinsic attenuation in the same way if the intrinsic attenuation is homogeneous in the medium. Even if the intrinsic attenuation is not homogeneous in the medium, the ratio of the coda and entire space energies strongly reflects scattering. The coda energy is more effectively generated when the scattering is large. Therefore, we can reasonably measure the scattering effect by using the ratio of the coda energy against the entire area energy.

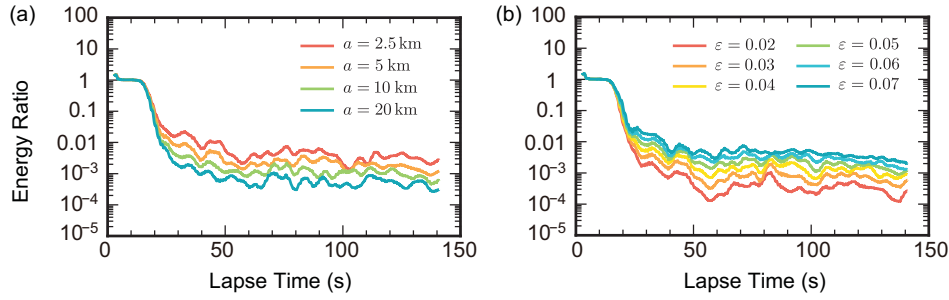


Figure 4. Lapse time dependence of the calculated energy ratio for event 1 for different a with fixed $\varepsilon = 0.05$ at the period band of 2 s–4 s (a). (b) Same as (a) but for different ε with fixed $a = 5$ km.

2.3 FD simulation

We conduct 3-D FD simulations to model the observed energy ratio and estimate statistical parameters of small-scale heterogeneities and the intrinsic attenuation. The background velocity structure is assumed to be the 1-D velocity structure used in the moment tensor estimation by the F-net (Kubo *et al.* 2002). We superimpose the 3-D fractional fluctuation ξ on the 1-D background velocity as

$$V(\mathbf{x}) = \begin{cases} V(z)[1 + \xi(\mathbf{x})] & \text{for } z < 33 \text{ km} \\ V(z) & \text{for } z > 33 \text{ km} \end{cases}, \quad (4)$$

where V is the P - or S -wave velocities and ξ is a random variable. The random fluctuation ξ is characterized by an exponential-type autocorrelation function as

$$\langle \xi(\mathbf{x}')\xi(\mathbf{x}' + \mathbf{x}) \rangle = \varepsilon^2 e^{-r/a}, \quad (5)$$

where r is the propagation distance, a is the correlation distance, and ε is the RMS fractional fluctuation. The angular bracket $\langle \dots \rangle$ indicates the ensemble average. The accuracy of the FD calculation is of the fourth order in space and the second order in time. The grid interval is 1 km in all directions, and the time interval is 20 ms. The numbers of the grid are 1536 and 512 for the two horizontal and vertical directions, respectively. We set the free surface boundary condition at the top of the medium and the absorbing boundary condition (Cerjan *et al.* 1985) at the other boundaries. The calculation is conducted on the Earth Simulator, which is a supercomputer managed by JAMSTEC. We adopt the MPI parallel computation for efficient calculations (e.g. Furumura & Chen 2004). We search the scattering and attenuation parameters in the crust that reproduce the observed spatiotemporal distribution of the seismic wave energy by changing scattering parameters (a and ε) and the intrinsic absorption parameter (Q).

3 RESULTS

First, we estimate the statistical parameters of the small-scale random fluctuation, a and ε , by using the energy ratio. The effects of the correlation distance and the RMS fluctuation on the lapse time dependence of the energy ratio are shown in Fig. 4. The energy ratio is 1 at the beginning because the upper limit of the integral of the energy ($\Delta_D(t)$) in eq. (2) is smaller than Δ_c , that is, E_T and E_C are the same. The energy ratio decreases with the lapsed time because the energy spherically spreads from the source. The area of the calculation of E_T , that is Δ_D , becomes large, while that of E_C is constant (Δ_c). At a fixed ε , a smaller a leads to a larger energy ratio (Fig. 4a). This means that the coda energy for the small correlation distance is larger than that for the large correlation distance. When we fix a , the energy ratio for the large ε is larger than that of the small ε (Fig. 4b). The combinations of smaller a and a fixed ε and

that of larger ε and a fixed a lead to a similar energy ratio curve. There is a trade-off between a and ε . Therefore, we cannot distinguish the effects of the correlation distance and the fluctuation from the analysis of the energy ratio.

We estimate the best-fit combination of a and ε by using the grid search. The misfit between the observed and calculated energy ratio is defined as

$$\text{misfit} = \sum_{i=1}^N \left[\frac{\log(\text{ER}^{\text{obs}}(t_i)) - \log(\text{ER}^{\text{cal}}(t_i))}{\log(\text{ER}^{\text{obs}}(t_i))} \right]^2, \quad (6)$$

where we set $t_1 = 50$ s and $t_N = 130$ s. The energy ratio is not stable at the early lapse time because the number of stations within the wave front is limited. Therefore, we use the energy ratio after the lapse time of 50 s. The energy ratio at later lapse time reflects the statistical averaged characteristics of the random fluctuation. We change a from 2.5 km to 20 km and ε from 0.02 to 0.07. We show the result of the grid search for event 1 in Fig. 5. The best-fit parameters are $(a, \varepsilon) = (2.5 \text{ km}, 0.04)$, $(2.5 \text{ km}, 0.05)$, and $(5 \text{ km}, 0.06)$ at period bands of 8–16 s, 4–8 s and 2–4 s, respectively. As we mentioned above, Fig. 5 shows the trade-off between a and ε . The trend of the lower misfit combinations of a and ε are not linear. According to the Born approximation (e.g. Chernov 1960), the scattering coefficient that represents the strength of the scattering is proportional to the power spectrum density function (PSDF) of random fluctuations (ξ). The PSDF of the exponential-type random medium is written as

$$P(m) = \frac{8\pi\varepsilon^2 a^3}{(1 + a^2 m^2)^2}, \quad (7)$$

where m is the wavenumber of the medium heterogeneity. The PSDF is proportional to ε^2/a for $am \gg 1$ and $\varepsilon^2 a^3$ for $am \ll 1$. At 8–16 s, misfit values are decreasing with the increase of a for $a \leq 5$ km. Conversely, misfit values increase with increasing a for $a \geq 10$ km. Therefore, the trend of the combination of lower misfit value may be controlled by the PSDF at each period band.

Fig. 6(a) shows the comparison of the observed and best-fit calculated energy ratios. The observed energy ratio is adequately modelled by the calculation at the lapse time between 50 and 130 s. At the period band of 2–4 s, the observed energy ratio is slightly larger than the calculated one at the lapse time between 20 and 50 s. Even if we set the smallest correlation distance and the largest fluctuation, this slight discrepancy does not decrease sufficiently. This may reflect the effect of the local scale deterministic structure, which is not taken into account in the calculation. Such effect is suppressed at the later lapse time, because we can use many stations covering all directions.

We also analyse events 2 and 3 by using the same calculation procedure. We assume that effects of the focal depth, radiation

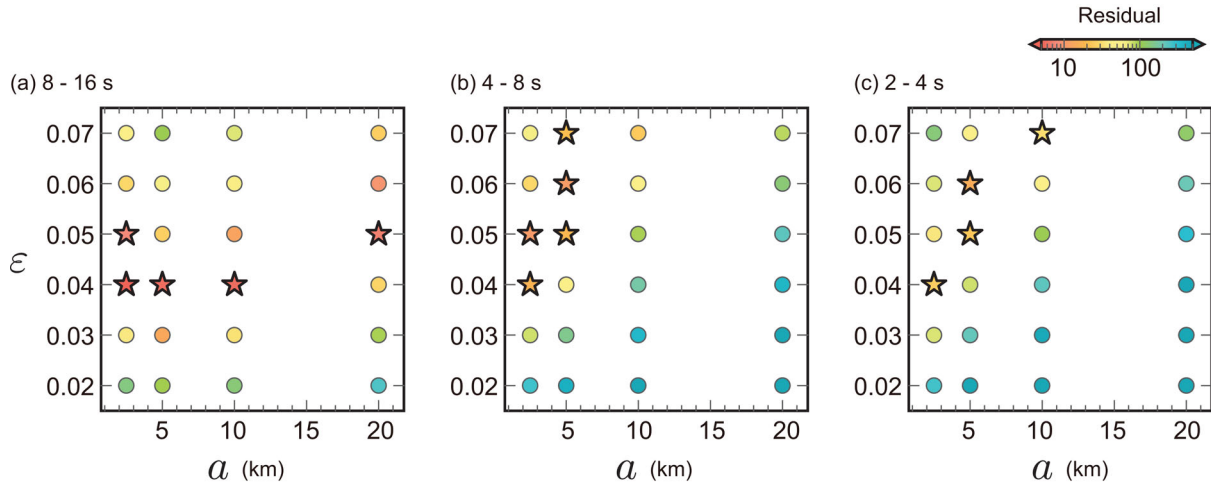


Figure 5. Misfit distribution for the combination of a and ε for event 1 at period bands of 8–16 s, 4–8 s, and 2–4 s. Star symbols indicate the misfit within 200 per cent of the minimum.

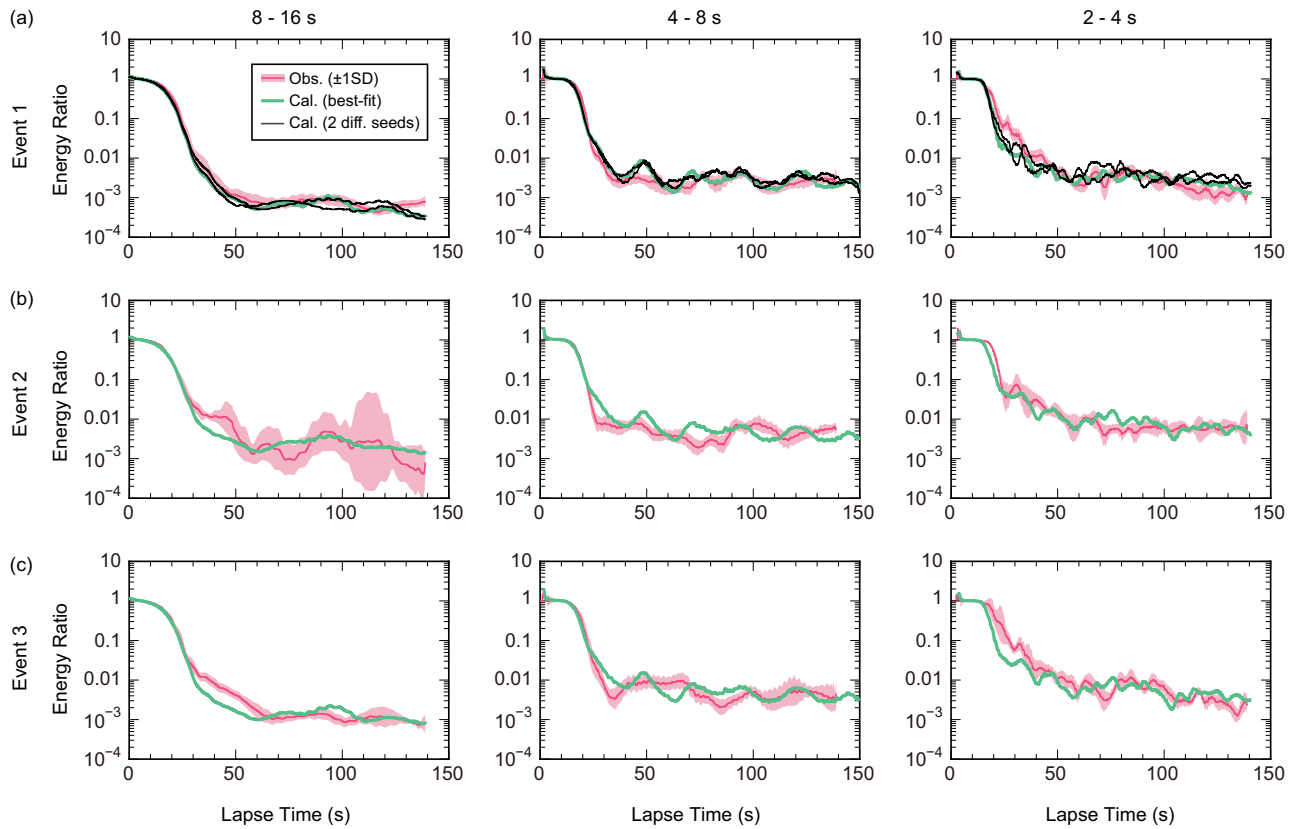


Figure 6. Comparison of the observed and best-fit calculated energy ratios for (a) event 1, (b) event 2, and (c) event 3. The observed energy ratio is indicated by a thin red line with ± 1 standard deviation (light red area). The thick green line indicates the best-fit calculated energy ratio. In (a), the energy ratios calculated with the best-fit parameters for different seeds are shown by thin black lines.

pattern, and magnitude on the energy ratio can be negligible. By using the same procedure of the grid search, we obtain the best-fit parameters as $(a, \varepsilon) = (10 \text{ km}, 0.07)$, $(2.5 \text{ km}, 0.07)$, and $(2.5 \text{ km}, 0.07)$ at period bands of 8–16 s, 4–8 s, and 2–4 s, respectively for event 2. The best-fit parameters for the event 3 are $(a, \varepsilon) = (2.5 \text{ km}, 0.06)$, $(2.5 \text{ km}, 0.07)$, and $(2.5 \text{ km}, 0.06)$ at period bands of 8–16 s, 4–8 s, and 2–4 s, respectively. The comparison between the observed and best-fit energy ratios for events 2 and 3 are shown in Figs 6(b) and (c).

The energy ratio is almost independent of the intrinsic attenuation, but the absolute values of the energies of the entire area and coda depend on both the statistical parameters and the intrinsic attenuation. The scattering effect is the redistribution of the energy. When scattered waves mainly consist of surface waves, the surface integral of the energy density on the ground is almost conserved if there is no intrinsic attenuation. Therefore, the decay rate of the energy with respect to the lapse time is strongly controlled by the intrinsic attenuation. This idea would be widely applicable to not

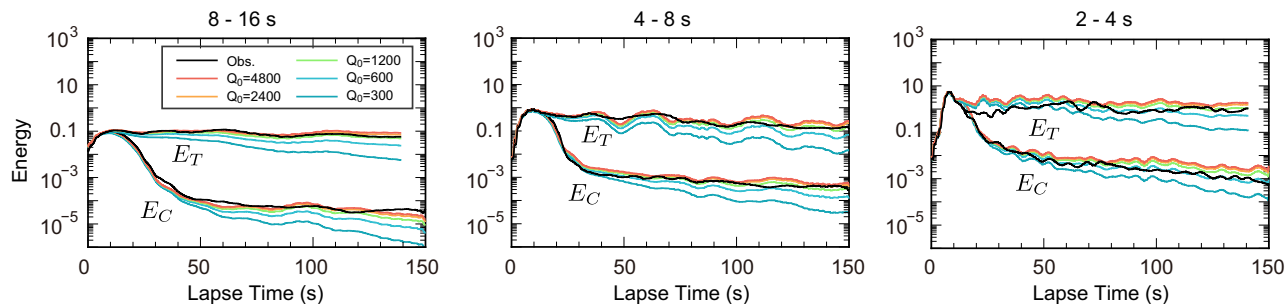


Figure 7. Comparison of the lapse time dependence of the observed and calculated energies of event 1 for different Q values at period bands of 8–16 s, 4–8 s and 2–4 s.

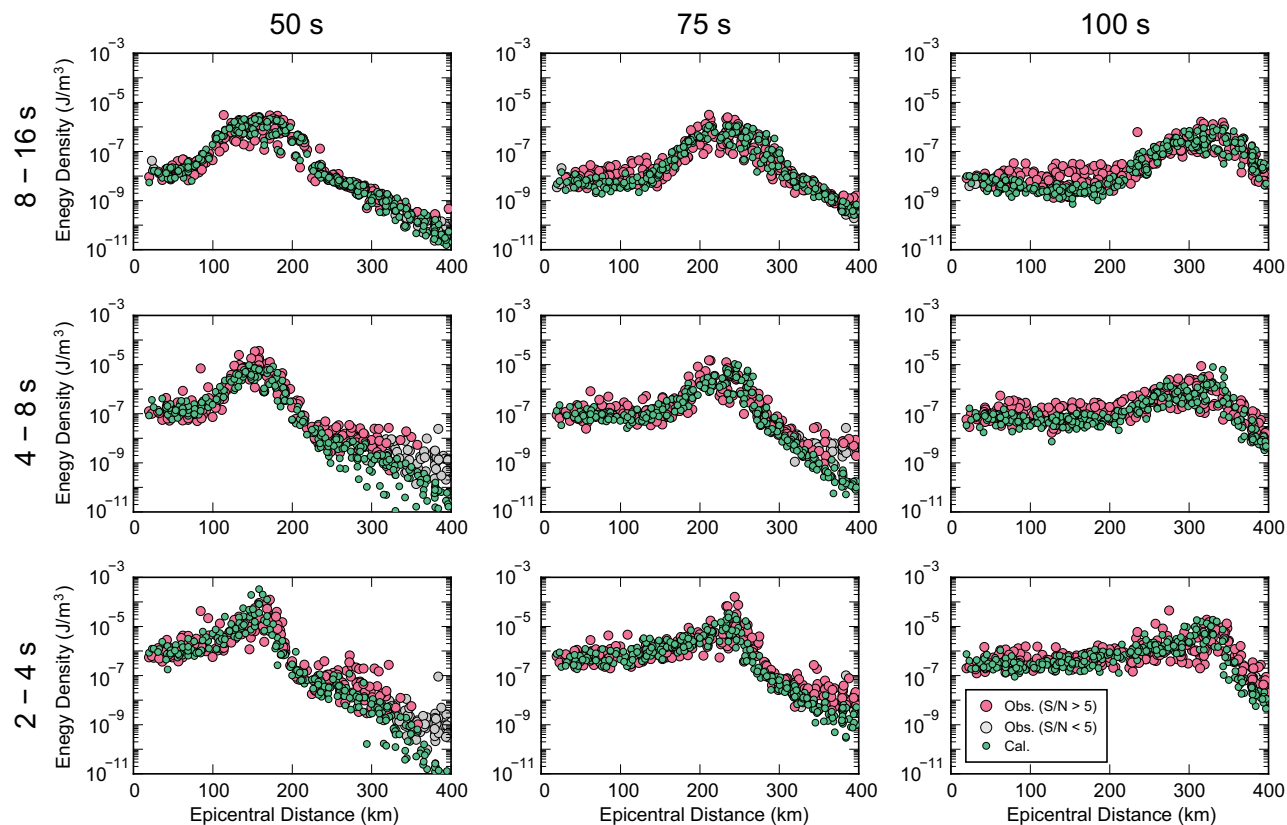


Figure 8. Snapshot of the epicentral distance variation of the energy densities of the observation (pink and grey) and the best-fit calculation (green) at the lapse times of 50 s (left), 75 s (centre), and 100 s (right) for event 1. The top, middle, and bottom panels show the period bands of 8–16 s, 4–8 s, and 2–4 s, respectively.

only seismic-wave scattering but also wave scattering problems, in general. For example, tsunami coda decay rate is strongly controlled by the intrinsic energy absorption due to sea-bottom friction (e.g. Saito *et al.* 2013b). We estimate the intrinsic attenuation by modelling the temporal change of the energy and using the best-fit statistical parameters. Fig. 7 shows the comparison between the observed and calculated energies for different intrinsic attenuations (Q values). In FD simulations, we adopt the frequency dependent Q as $Q = Q_0/f/f_0$, where $f_0 = 1$ Hz is the reference frequency and Q_0 is the Q value at the reference frequency. The attenuation is faster for smaller Q_0 value. The best-fit Q values are 225 at all period bands. We note that the rate of decrease of E_T and E_C are the same at the same Q value, and the effect of Q is cancelled by taking their ratio.

Figs 8–11 show the comparison between observed and best-fit calculated energy density distributions. The calculated energy density correctly models the observed one. There is slight discrepancy

between the calculated and observed energy density around the arrival of the peak amplitude. This may be due to the fact that our model consists of a 1-D velocity structure with small-scale 3-D random fluctuations in the crust. The deterministic 3-D velocity structure, such as the inhomogeneous depth of the Moho, is necessary especially for the energy density around the direct wave front (e.g. Furumura *et al.* 2014; Takemura *et al.* 2015).

4 DISCUSSION

4.1 Effect of the realizations of random media

When we make the random fluctuation, we assume a and ε to characterize the PSDF and a seed to generate random numbers. By using different seeds, we can generate the different realizations

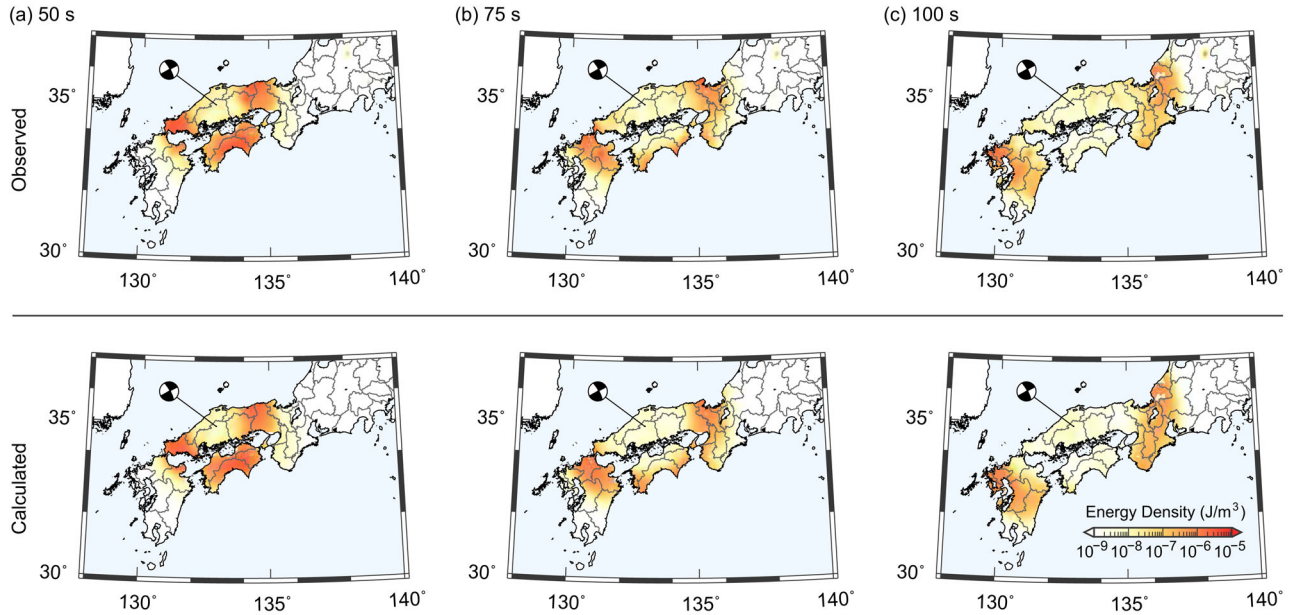


Figure 9. Snapshot of the spatial distribution of the energy densities of the observation (upper three panels) and the best-fit calculation (lower three panels) at the period band of 8–16 s at the lapse times of (a) 50 s, (b) 75 s, and (c) 100 s for event 1.

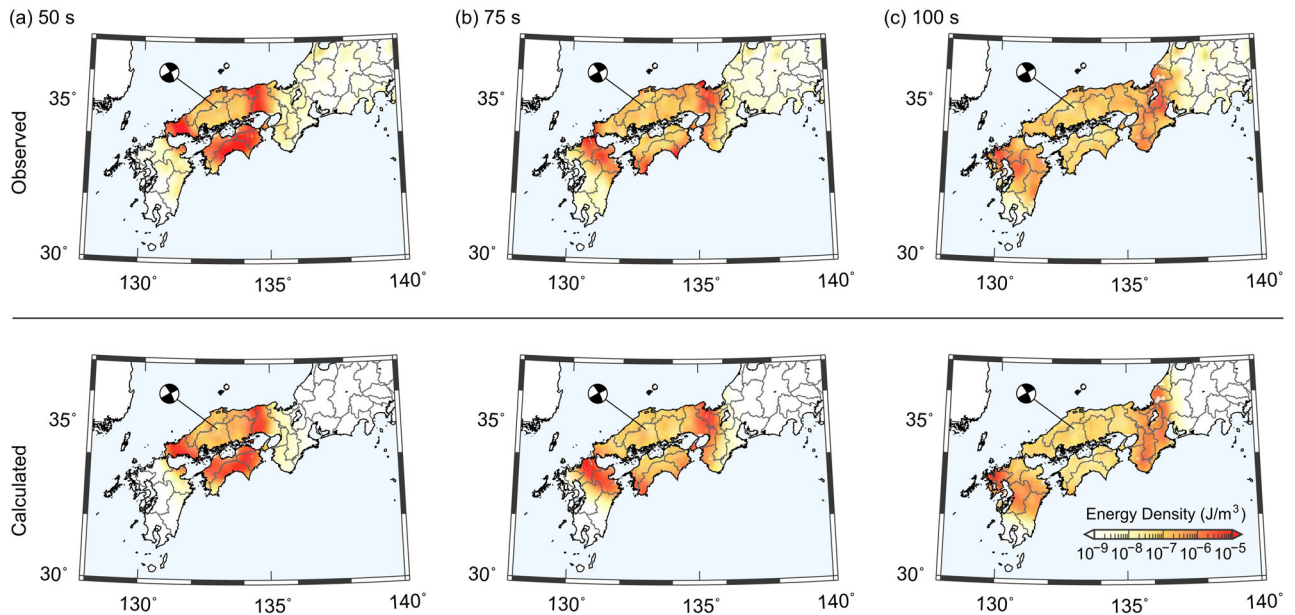


Figure 10. Same as Fig. 9 for the period band of 4–8 s.

of the random medium by keeping the same statistical properties. The theoretical meaning of the ensemble average in the statistical method is the average over different realizations of random media. For the grid search, we used a specific realization. We investigate the effect of the realization on the calculated energy ratio. Fig. 6(a) shows the calculated energy ratios in two different realizations of random media where the best-fit parameters are the same. The energy ratios calculated with different random realizations are almost the same, though there is a small difference in the fluctuation. In our analysis, we use stations that cover all the directions from the source. Therefore, the effect of the random realization is insignificant, and we can obtain the value close to the ensemble average in our analysis even if we use only a specific realization.

4.2 Effect of the heterogeneity in the mantle

We superimposed the 3-D random heterogeneity on the crust only because it is considered that the heterogeneity in the mantle is much weaker than that in the crust (e.g. Lee *et al.* 2003; Margerin & Nolet 2003; Shearer & Earle 2004). Moreover, sometimes the mantle is treated as a homogeneous medium (e.g. Margerin *et al.* 1999). We check the effect of the heterogeneity in the mantle by superimposing the 3-D random heterogeneity as $a = 8$ km and $\varepsilon = 0.5$ per cent (Shearer & Earle 2004). Fig. 12 shows the comparison of the energy ratios for the cases of the 3-D random heterogeneity in the crust only and that in the crust and the mantle. There is a slight difference at the period band of 2–4 s. The energy ratios at the period bands of 8–16 s and 4–8 s are not affected. Therefore,

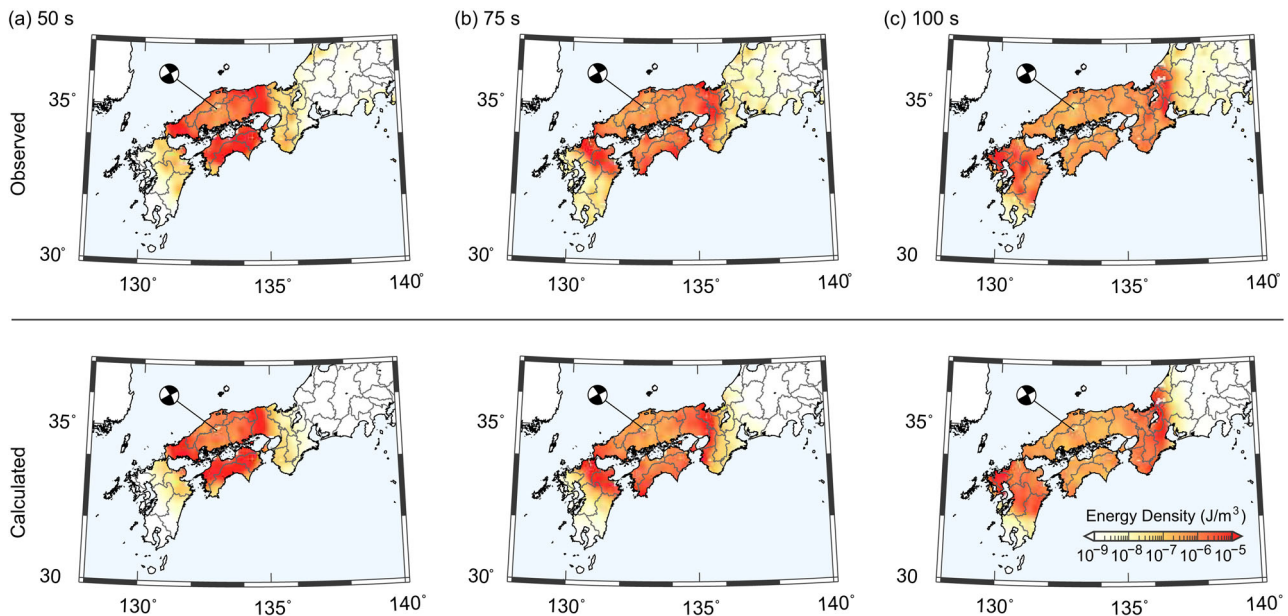


Figure 11. Same as Fig. 9 for the period band of 2–4 s.

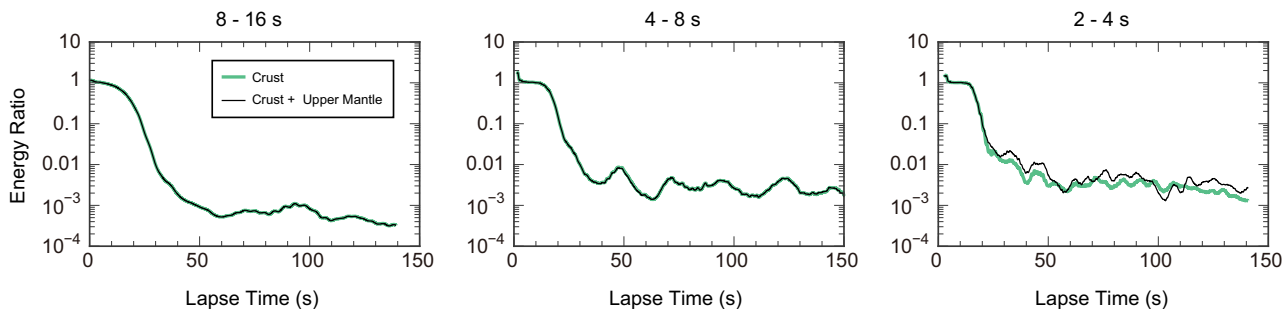


Figure 12. Comparison of the energy ratios of the best-fit model (heterogeneities only in the crust) and the heterogeneous mantle model at period bands of 8–16 s, 4–8 s and 2–4 s for event 1. For the case of the heterogeneous mantle mode, we added the random heterogeneity in the upper mantle in addition to the crust.

we can say that if the heterogeneity in the mantle is weak, our result mainly reflects the heterogeneity in the crust, especially at longer period bands.

4.3 Comparison with previous studies

4.3.1 Random heterogeneity in the lithosphere

We plot the PSDFs of small-scale heterogeneities estimated by previous studies compiled by Sato *et al.* (2012) in Fig. 13 (grey line). The results of Takemura *et al.* (2009) and Kobayashi *et al.* (2015) are also plotted. They estimated the PSDF by focusing on the distortion of the *P*- and *S*-wave radiation patterns in the same region as this study. Most of the previous studies analyse short-period seismograms because the effect of small-scale heterogeneities is significant for short periods. In most cases, the analysed period range is shorter than 4 s, and the PSDF of random heterogeneities whose wavenumber range is higher than 0.4 km^{-1} is estimated. For the wavenumber range higher than 0.4 km^{-1} , the corner of the PSDF is not clearly observed and the shape of the PSDF can be modelled by the power-law decay spectrum. By assuming the power-law decay, the best-fit curve for the PSDFs of previous studies can be written as

$$P(m) = 0.015m^{-3.9} \quad \text{for } m > 0.4 \text{ km}^{-1}, \quad (8)$$

where the estimation in the mantle and our results are not included. The best-fit power law decay is shown in Fig. 13 in the orange dotted line.

We show the PSDF calculated by using the best-fit combination of a and ε with the error in Fig. 13. We obtain the error of the best-fit parameters by accepting the combination of a and ε whose misfit value is within twice of the best-fit value. In this error estimation, the results of all three events are included. The analysed period range of this study (2–16 s) is longer than that of previous studies. When we assume that the *S*-wave velocity is 4 km s^{-1} , our analysed range corresponds to the wavenumber range between 0.1 and 0.8 km^{-1} . Our estimated PSDF at the wavenumber range between 0.4 and 0.8 km^{-1} overlaps with that of previous studies. In addition, we estimate the PSDF for the wavenumber range between 0.1 and 0.4 km^{-1} , which is not sufficiently reported so far. According to previous studies, the PSDF can be modelled by the power-law decay as in eq. (8) in the wide wavenumber range of 0.4 – 50 km^{-1} . However, we can see the corner around the wavenumber of 0.4 km^{-1} by adding our result. We calculate the best-fit PSDF for all the reported values including our result, except for the estimation of the mantle heterogeneities (Shearer & Earle 2004). We use the least-squares method in log-log space and estimate a and ε by assuming an exponential-type random fluctuation in eq. (7). The best-fit parameters are $a = 3.1 \text{ km}$ and $\varepsilon = 0.05$ (green dashed line in Fig. 13). The corner of the PSDF

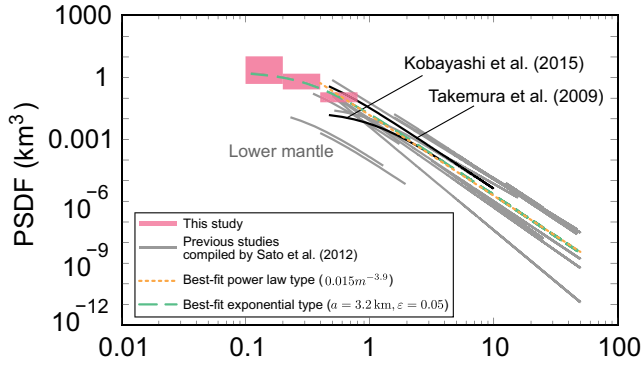


Figure 13. Comparison of power spectral density functions (PSDFs) estimated in this study with those of previous studies. We calculate the PSDF by using the estimated parameters, a and ε , whose misfit values are within 200 per cent of the best-fit values. Results of all three events are included. Grey lines are reported PSDFs compiled by Sato *et al.* (2012). We check the analysed wavenumber range of each study and plot the PSDF only at that range. Black lines indicate the results of Takemura *et al.* (2009) and Kobayashi *et al.* (2015). The best-fit power law decay curve and exponential-type PSDF are plotted by orange dotted and green dashed lines, respectively.

can be recognized because we analysed longer period range. The corner of the PSDF is determined by the correlation distance. The scattering regime is controlled by the relationship between a and the wavenumber of the wave (k). When $ak \gg 1$, the forward scattering is dominant. In this case, effects of the travel time fluctuation and the envelope broadening are important. Conversely, when $ak \ll 1$, the scattering is isotropic. In this case, the coda excitation is significant. Therefore, knowing the corner of the PSDF is important for evaluating the scattering effect at a given wavenumber. There is a possibility that the location of the corner depends on the analysis method. It is necessary to analyse the wide wavenumber range by using the same method to validate the shape of the PSDF around its corner.

4.3.2 Total scattering coefficient

We calculate the total scattering coefficient (g_0), which represents the power of the scattering per unit volume. Based on the Born approximation, g_0 for exponential-type random media can be written as (Sato *et al.* 2012, Chap. 4)

$$g_0 = \frac{8\varepsilon^2 a^3 k^4}{1 + 4a^2 k^2}, \quad (9)$$

where k is the wavenumber of the wave. The inverse of the total scattering coefficient corresponds to the mean free path of the scattering in the inhomogeneous medium. The medium having large g_0 strongly generates the scattered waves. In Fig. 14, we show the comparison of our estimated g_0 and those reported in previous studies. As is the case for the PSDF, there are many estimations of g_0 in the short-period range, while the number of studies in the long-period range is few. Our estimation range might connect the gap between the studies of long and short periods. We note that we introduced random small-scale heterogeneities only in the crust and assumed that the mantle is transparent. Therefore, our estimated values may mainly reflect small-scale heterogeneities in the crust.

4.3.3 Quality factor

We show the estimated Q with the results of previous studies in Fig. 15. In our FD simulation, we assume that the Q values for

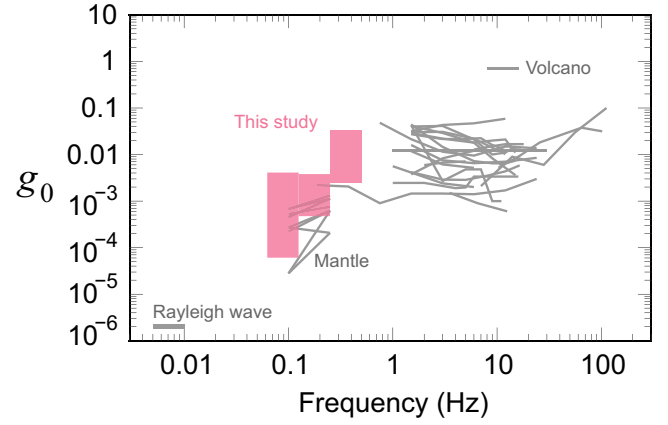


Figure 14. Comparison of g_0 values estimated in this study (red area) with those of previous studies compiled by Sato *et al.* (2012) (grey lines). We calculate the g_0 by using the estimated parameters, a and ε , whose misfit values are within 200 per cent of the best-fit values. Results of all 3 events are included.

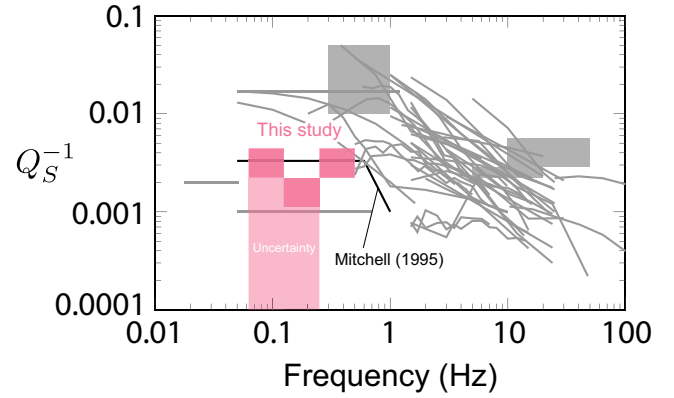


Figure 15. Comparison of the estimated intrinsic attenuation (red area) with Q_s of previous studies compiled by Sato *et al.* (2012) (grey lines). At period bands of 8–16 s and 4–8 s, we cannot constrain the upper limit of Q due to the weak attenuation (Fig. 7). Therefore, we plot the light red area as the uncertainty, where Q values are higher than our investigated range.

P - and S -waves are the same and proportional to the frequency. As shown in Fig. 7, the attenuation of the energy is weak, so the highest limit of Q is not well resolved. Our result is close to the Q value in the stable upper crust obtained by the analysis of the Rayleigh wave (Mitchell 1995). In our period band, surface waves might be dominant.

5 CONCLUSIONS

We have analysed the spatiotemporal variation of the energy of the seismic wave observed by the dense seismic network at period bands of 8–16 s, 4–8 s and 2–4 s in southwestern Japan. The spatial variation of the energy shows the uniform distribution around the source, in other words, coda energy does not depend on the distance from the epicentre. This is the typical characteristic of the short-period case due to the scattering by small-scale heterogeneities. By defining the coda energy and taking the ratio of the coda energy to the entire area energy, we cancelled the effect of the intrinsic attenuation and estimated the statistical parameters of small-scale heterogeneities in the crust, which control scattering properties. We numerically calculated the energy ratio by using 3-D FD simulations. We changed a and ε to estimate the best-fit

combination. The PSDF of $P(m) = 8\pi\varepsilon^2 a^3 / (1 + a^2 m^2)^2$, where $\varepsilon = 0.05$ and $a = 3.1$ km, can reproduce the spatial and temporal distribution of the energy for a wide frequency range from 0.06 to 0.5 Hz. This PSDF of the fractional velocity fluctuation in the crust partly overlaps with the results of past studies. The corner was unclear in previous studies, because they analysed only high frequency seismic energy. In addition, by modelling the temporal decay of the energy, we estimated the intrinsic attenuation. The best-fit Q_0 values are 225 at a period band of 2–16 s. The advantage of our study is that we do not need to make many assumptions compared to the studies based on statistical theory. Furthermore, we are able to reproduce the energy distribution at lower wave frequency and estimate lower wavenumber heterogeneities.

ACKNOWLEDGEMENTS

We are grateful to an anonymous reviewer and Julien Chaput for their careful review and valuable suggestions. We would like to thank Takashi Furumura for providing the original code of the FD simulation. Computations were conducted on the Earth Simulator at the Japan Agency for Marine-Earth Science and Technology (JAMSTEC) under the support of a joint research project between the Earthquake Research Institute, the University of Tokyo, and the Center of Earth Information Science and Technology entitled ‘Numerical simulations of seismic- and tsunami-wave propagation in 3-D heterogeneous earth’. This study was supported by the Joint Usage / Research Center program of Earthquake Research Institute, the University of Tokyo (#2015-B-01).

REFERENCES

- Aki, K., 1969. Analysis of the seismic coda of local earthquakes as scattered waves, *J. geophys. Res.*, **74**(2), 615–631.
- Asano, Y. & Saito, T., 2011. Scattering coefficient estimated from the observed energy density of S coda, in *SSJ Fall Meeting*, C12-08.
- Cerjan, C., Kosloff, D., Kosloff, R. & Reshef, M., 1985. A nonreflecting boundary condition for discrete acoustic and elastic wave equations, *Geophysics*, **50**, 705–708.
- Chaput, J., Campillo, M., Aster, R., Roux, P., Kyle, P., Knox, H. & Czoski, P., 2015. Multiple scattering from icequakes at Erebus volcano, Antarctica: implications for imaging at glaciated volcanoes, *J. geophys. Res.*, **120**, 1129–1141.
- Chernov, L.A., 1960. *Wave Propagation in a Random Medium*, McGraw-Hill.
- De Rosny, J. & Roux, P., 2001. Multiple scattering in a reflecting cavity: Application to fish counting in a tank, *J. acoust. Soc. Am.*, **109**, 2587–2597.
- Fehler, M., Hoshihara, M., Sato, H. & Obara, K., 1992. Separation of scattering and intrinsic attenuation for the Kanto-Tokai region, Japan, using measurements of S -wave energy versus hypocentral distance, *Geophys. J. Int.*, **108**, 787–800.
- Furumura, T. & Chen, L., 2004. Large scale parallel simulation and visualization of 3D seismic wavefield using the Earth Simulator, *Comput. Model. Eng. Sci.*, **6**, 153–168.
- Furumura, T., Hong, T.-K. & Kennett, B., 2014. L_g wave propagation in the area around Japan: observations and simulations, *Prog. Earth Planet. Sci.*, **1**, 10, doi:10.1186/2197-4284-1-10.
- Hoshihara, M., 1993. Separation of scattering attenuation and intrinsic absorption in Japan using the multiple lapse time window analysis of full seismogram envelope, *J. geophys. Res.*, **98**, 15 809–15 824.
- Kobayashi, M., Takemura, S. & Yoshimoto, K., 2015. Frequency and distance changes in the apparent P -wave radiation pattern: effects of seismic wave scattering in the crust inferred from dense seismic observations and numerical simulations, *Geophys. J. Int.*, **202**, 1895–1907.
- Kubo, A., Fukuyama, E., Kawai, H. & Nonomura, K., 2002. NIED seismic moment tensor catalogue for regional earthquakes around Japan: quality test and application, *Tectonophysics*, **356**, 23–48.
- Larose, E., Margerin, L., van Tiggelen, B. & Campillo, M., 2004. Weak localization of seismic waves, *Phys. Rev. Lett.*, **93**, doi:10.1103/PhysRevLett.93.048501.
- Lee, W.S., Sato, H. & Lee, K., 2003. Estimation of S -wave scattering coefficient in the mantle from envelope characteristics before and after the S_cS arrival, *Geophys. Res. Lett.*, **30**, 2248, doi:10.1029/2003GL018413.
- Maeda, T., Obara, K., Furumura, T. & Saito, T., 2011. Interference of long-period seismic wavefield observed by the dense Hi-net array in Japan, *J. geophys. Res.*, **116**, B10303, doi:10.1029/2011JB008464.
- Margerin, L. & Nolet, G., 2003. Multiple scattering of high-frequency seismic waves in the deep Earth: PKP precursor analysis and inversion for mantle granularity, *J. geophys. Res.*, **108**(B11), 2514, doi:10.1029/2003JB002455.
- Margerin, L., Campillo, M., Shapiro, N. & van Tiggelen, B., 1999. Residence time of diffuse waves in the crust as a physical interpretation of coda Q : application to seismograms recorded in Mexico, *Geophys. J. Int.*, **138**, 343–352.
- Margerin, L., Campillo, M. & van Tiggelen, B., 2001. Coherent backscattering of acoustic waves in the near field, *Geophys. J. Int.*, **145**, 593–603.
- Mitchell, B., 1995. Anelastic structure and evolution of the continental crust and upper mantle from seismic surface wave attenuation, *Rev. Geophys.*, **33**, 441–462.
- Obara, K., Kasahara, K., Hori, S. & Okada, Y., 2005. A densely distributed high-sensitivity seismograph network in Japan: Hi-net by National Research Institute for Earth Science and Disaster Prevention, *Rev. Sci. Instrum.*, **76**, 021301, doi:10.1063/1.1854197.
- Okada, Y., Kasahara, K., Hori, S., Obara, K., Sekiguchi, S., Fujiwara, H. & Yamamoto, A., 2004. Recent progress of seismic observation network in Japan—Hi-net, F-net, K-NET and KiK-net—, *Earth Planets Space*, **56**, xv–xviii.
- Ritter, J., Shapiro, S. & Schechinger, B., 1998. Scattering parameters of the lithosphere below the Massif Central, France, from teleseismic wavefield records, *Geophys. J. Int.*, **134**, 187–198.
- Saito, K., Kawahara, J. & Saito, T., 2013a. On estimation of scattering coefficient and intrinsic absorption from spatial distribution of seismic energy, in *SSJ Fall Meeting*, C32-05.
- Saito, T., Sato, H., Ohtake, M. & Obara, K., 2005. Unified explanation of envelope broadening and maximum-amplitude decay of high-frequency seismograms based on the envelope simulation using the Markov approximation: forearc side of the volcanic front in northeastern Honshu, Japan, *J. geophys. Res.*, **110**, B01304, doi:10.1029/2004JB003225.
- Saito, T., Inazu, D., Tanaka, S. & Miyoshi, T., 2013b. Tsunami coda across the Pacific Ocean following the 2011 Tohoku-Oki Earthquake, *Bull. seism. Soc. Am.*, **103**, 1429–1443.
- Sato, H., Fehler, M. & Maeda, T., 2012. *Seismic Wave Propagation and Scattering in the Heterogeneous Earth*, 2nd edn, Springer.
- Shearer, P. & Earle, P., 2004. The global short-period wavefield modelled with a Monte Carlo seismic phonon method, *Geophys. J. Int.*, **158**(3), 1103–1117.
- Shiomi, K., Obara, K. & Kasahara, K., 2005. Amplitude saturation of the NIED Hi-net waveforms and simple criteria for recognition (in Japanese), *Zisin 2*, **57**, 451–461.
- Takemura, S., Furumura, T. & Saito, T., 2009. Distortion of the apparent S -wave radiation pattern in the high-frequency wavefield: Tottori-Ken Seibu, Japan, earthquake of 2000, *Geophys. J. Int.*, **178**, 950–961.
- Takemura, S., Akatsu, M., Masuda, K., Kajikawa, K. & Yoshimoto, K., 2015. Long-period ground motions in a laterally inhomogeneous large sedimentary basin: observations and model simulations of long-period surface waves in the northern Kanto Basin, Japan, *Earth Planets Space*, **67**, 33, doi:10.1186/s40623-015-0201-7.
- Wegler, U. & Lühr, B., 2001. Scattering behaviour at Merapi volcano (Java) revealed from an active seismic experiment, *Geophys. J. Int.*, **145**, 579–592.
- Yamamoto, M. & Sato, H., 2010. Multiple scattering and mode conversion revealed by an active seismic experiment at Asama volcano, Japan, *J. geophys. Res.*, **115**, B07304, doi:10.1029/2009JB007109.